PCCP

Accepted Manuscript

ROYAL SOCIETY OF CHEMISTRY

www.rsc.org/pccp

Cite this: DOI: 10.1039/c0xx00000x

www.rsc.org/xxxxxx

ARTICLE TYPE

Tunable upconversion luminescence in self-crystallization Er^{3+}: $K(Y_{1-x}Yb_x)_3F_{10}$ nano-glass-ceramics

Daqin Chen[*,a,b], Yang Zhou[a], Zhongyi Wan[a], Hua Yu, Hongwei Lu, Zhenguo Ji[*,a], Ping Huang[*,b]

Received (in XXX, XXX) Xth XXXXXXXXX 20XX, Accepted Xth XXXXXXXXX 20XX

DOI: 10.1039/b000000x

$K(Y_{1-x}Yb_x)_3F_{10}$ (x=0-1) solid-solution nanocrystals embedded glass ceramics were fabricated via glass self-crystallization. Using Eu^{3+} as structural probe, the partition of lanthanide activators into $K(Y_{1-x}Yb_x)_3F_{10}$ lattice was evidenced. As a consequence, color-tunable upconversion luminescence from green to red was easily realized by modifying Yb^{3+} content in the Er^{3+}-doped nano-glass-ceramics.

Currently, there is a great interest in optical materials doped with lanthanide (Ln^{3+}) activators for efficient frequency upconversion (UC) from infrared to visible radiation. This is because a visible source pumped by a near-infrared (NIR) laser is useful for high-capacity data storage, sensor, all-solid compact laser, three-dimensional display, photovoltaic device as well as biomedical image [1-6]. It is well known that Ln^{3+} UC performance is closely related to the host matrices and their crystal structures. Among various host materials, transparent oxyfluoride glass ceramics (GCs) might be an ideal choice, which combine the favorable properties from both fluoride crystal and oxide glass matrix, i.e., low phonon energy and high mechanical, chemical stabilities[7]. Such nanostructured composite is achieved by controlled crystallization of the precursor glass with appropriate chemical composition, and the key factor for the efficient luminescence is the partition of the optically active Ln^{3+} ions into the precipitated fluoride nanocrystals (NCs).

So far, several studies on fluoride nanophases, such as PbF_2, YF_3, CaF_2, $NaYF_4$, $BaYF_5$, $LiYbF_4$, $NaGdF_4$ and KYb_2F_7 embedded GCs have been reported [8-19]. In these systems, the entering of the Ln^{3+} dopants into host is mainly realized by diffusion of Ln^{3+} ions from glass matrix to the precipitated crystals, which are highly affected by the diffusion activation energy and diffusion coefficient of Ln^{3+} in glass. At relatively low crystallization temperature, the low diffusion coefficient of Ln^{3+} in glass impedes their incorporation into crystals, while at high crystallization temperature the rapid growth of NCs obviously degrades the transparency of GCs, which are harmful to their optical performance. In this letter, by appropriately designing oxyfluoride glass composition, cubic $K(Y_{1-x}Yb_x)_3F_{10}$ solid-solution NCs embedded GCs were successfully fabricated for the first time. Different to the cases previously reported, GCs were directly formed via self-crystallization during melt-quenching, where Ln^{3+} dopants were demonstrated to incorporate into crystalline lattice. As a result, tunable upconversion luminescence can be easily realized in Er^{3+}: $K(Y_{1-x}Yb_x)_3F_{10}$ NCs embedded GC by simply modifying Y^{3+}/Yb^{3+} ratio.

Table 1 Nominal and actual composition (mol%) of GC3

Element	Nominal	Actual
Si	19.29	21.01
Al	6.44	6.89
K	10.61	9.02
Y	0.96	0.87
Yb	0.96	0.83
O	51.13	53.27
F	10.61	8.11

The material was prepared with the following composition (in mol%): $60SiO_2$-$10Al_2O_3$-$9K_2O$-15KF-(6-m)YF_3-mYbF_3 (m=0, 1, 3, 6). The 0.1 mol% Ln^{3+}-doping was realized by adding appropriate amount of EuF_3 or ErF_3. The chemicals were mixed thoroughly and melted in a covered platinum crucible at 1600 °C for 30 min in the ambient atmosphere. The melt was then poured into a 300 °C pre-heated copper mold and cooled down naturally to room temperature to form GC through self-crystallization (denoted as GC0, GC1, GC3 and GC6 for m=0, 1, 3 and 6 respectively). As a comparison, the specially designed amorphous glass with the composition of $60SiO_2$-$15Al_2O_3$-$9K_2O$-10KF-$6YbF_3$ was also prepared. This glass will not crystallize during melt-quenching.

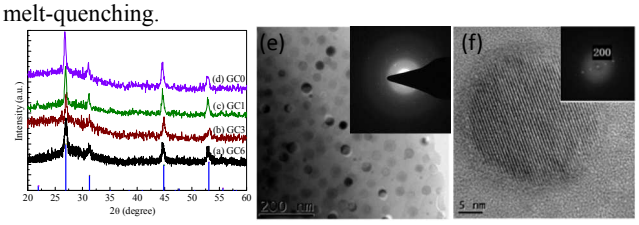

Figure 1 (a-d) XRD patterns of self-crystallization GCs; bars represent cubic KYb_3F_{10} crystal data (JCPDS No. 27-0462). (d) TEM image and SAED pattern of GC6 ($60SiO_2$-$10Al_2O_3$-$9K_2O$-15KF-$6YbF_3$); (e) HRTEM micrograph of an individual NC in GC6, inset shows the corresponding fast Fourier transform pattern.

As tabulated in Table 1, X-ray photoelectron spectroscopy (XPS) measured actual composition of GC3 sample (in mol%), together with its nominal composition ($60SiO_2$-$10Al_2O_3$-$9K_2O$-15KF-$3YF_3$-$3YbF_3$), is provided. Noticeably, compared with the

nominal ones, the actual contents of K, Y, Yb and F elements are more or less reduced, which is due to the thermal evaporation of the fluoride raw materials during high temperature melting. Fortunately, the Y/Yb ratio keeps almost unchanged after melting. X-ray diffraction (XRD) pattern of GC6 (Figure 1a) shows intense diffraction peaks assigned to cubic KYb_3F_{10} crystals (JCPDS No. 27-0462). With gradual increase of Y^{3+} content into the glass, similar XRD patterns for GC3 and GC1 and (Figure 1b-1c) are observed. When Yb^{3+} ions are totally replaced by Y^{3+} ones in the GC0 sample, pure cubic phase KY_3F_{10} (JCPDS No. 15-5135)[20-21] is detected. These results confirm the formation of cubic $K(Y_{1-x}Yb_x)_3F_{10}$ (x=0-1) solid-solution NCs in the glass matrix. The mean size of the crystals was calculated to be about 25 nm by the Scherrer formula. Transmission electron microscopy (TEM) image of GC6 sample (Figure 1e) demonstrates that nanoparticles sized 20-30 nm are distributed homogeneously among the glass matrix with their selected area electron diffraction (SAED) rings well indexed to the cubic KYb_3F_{10}. The detailed lattice structure of an individual NC in GC6 is revealed by the high-resolution TEM (HRTEM) micrograph shown in Figure 1f. Similar results can be found for GC0, GC1 and GC3 samples (no shown here).

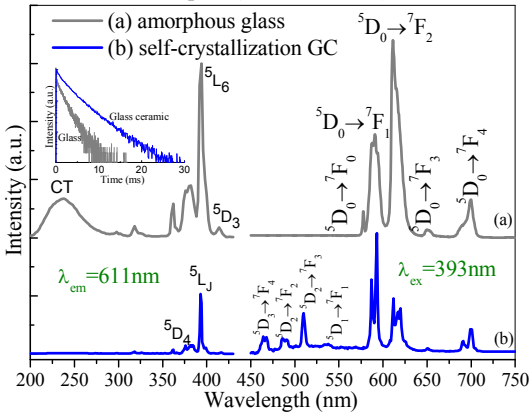

Figure 2 Excitation (λ_{em}=611 nm) and emission (λ_{ex}=393 nm) spectra of the Eu^{3+} doped amorphous glass (a) and GC6 sample (b); inset shows the decay curves of the Eu^{3+} $^5D_0$ state for the glass and GC6 samples.

Room temperature excitation and emission spectra of the self-crystallization KYb_3F_{10} GC6 sample doped with Eu^{3+} as structural probe are presented in Figure 2. As a comparison, the excitation/emission spectra of Eu^{3+} doped amorphous glass with the designed composition of $60SiO_2$-$15Al_2O_3$-$9K_2O$-$10KF$-$6YbF_3$ were also provided. For the amorphous glass, the excitation spectrum for the 611 nm emission of Eu^{3+}:$^5D_0\rightarrow{}^7F_2$ transition consists of several characteristic Eu^{3+} excitation peaks of the transitions from the $^7F_0$ ground state to the indexed excited states and the broad excitation band at 238 nm corresponding to the O^{2-}-Eu^{3+} charge transfer (CT). Interestingly, the CT band in the glass ceramic sample is much weaker than that of the amorphous glass. The disappearance of this O^{2-}-Eu^{3+} CT band in the glass ceramics is attributed to the incorporation of Eu^{3+} into $K(Y_{1-x}Yb_x)_3F_{10}$ fluoride crystal where the nearest coordination ions for Eu^{3+} are F^- not O^{2-}.The emission spectra for the glass and glass ceramic under 393 nm excitation exhibit the bands of the transitions from the excited ^5D_J level to the lower ^7F_J levels of Eu^{3+}. The emission bands of the glass are inhomogeneouly broadened, while those of the glass ceramic become remarkably structured in a way similar to the case of the Eu^{3+} doped crystal [22-23]. The "Stark splits" of the emission bands are more obvious in the glass ceramics than those in the glass due to the incorporation of Eu^{3+} into crystalline phase environment. Impressively, the luminescence originated from the $^5D_{1,2,3}$ levels appears in the glass ceramic. All these results confirm the existence of Eu^{3+} ions in low-phonon-energy crystalline environment, i.e., partitioned into KY_3F_{10} lattice, which is further verified by the much longer decay time of the glass ceramic than that of the precursor glass, as shown in the inset of Figure 2. The intensity ratio of $^5D_0\rightarrow{}^7F_2$ and $^5D_0\rightarrow{}^7F_1$ transitions is determined by the symmetry of the crystal sites in which Eu^{3+} ions are located. From the emission spectra, the ratio is evaluated to be 1.76 and 0.88 for the glass and glass ceramic respectively. The intensity of the magnetic dipolar $^5D_0\rightarrow{}^7F_1$ transition does not depend on the ligand field of Eu^{3+}, while the electric dipolar $^5D_0\rightarrow{}^7F_2$ transition is known to be forbidden in the centrosymmetric environment [24]. Therefore, the decrease of the ratio value after self-crystallization is related to the increase in the symmetry of the ligand field for Eu^{3+} incorporated in KYb_3F_{10} host by substituting Yb^{3+}.

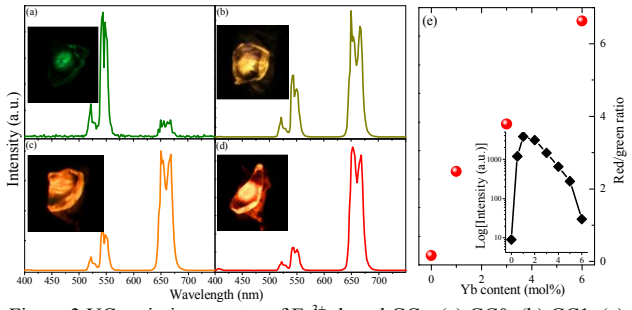

Figure 3 UC emission spectra of Er^{3+}-doped GCs: (a) GC0, (b) GC1, (c) GC3 and (d) GC6; inset is the corresponding UC luminescent photograph. (e) the dependence of red/green ratio on the Yb^{3+} content, inset show the impact of Yb^{3+} content on the integrated UC intensity of the sample.

UC emission spectra of the Er^{3+}-doped GCs containing $K(Y_{1-x}Yb_x)_3F_{10}$ solid-solution NCs are presented in Figure 3a-3d. Under 980 nm NIR laser excitation, all the spectra exhibit both green (~545 nm) and red (~650 nm) emission bands originated from $^2H_{11/2}$, $^4S_{3/2}\rightarrow{}^4I_{15/2}$ and $^4F_{9/2}\rightarrow{}^4I_{15/2}$ transitions of Er^{3+} respectively. Impressively, the red to green emission ratio enhances gradually with increase of Yb^{3+} content in the solid-solution NCs (Figure 3e), resulting in the color tunable luminescence from green to yellow and finally to red in the present GC samples. In addition, it is found the integrated UC emission intensity gradually enhances with increase of Yb^{3+} content from 0 to 1 mol%, and then monotonously decreases when further increasing Yb^{3+} content, as revealed in the inset of Figure 3e. The intensity of Er^{3+} doped GC1 with the optimal Yb^{3+} content (1 mol%) is about 450 times higher than that of GC0 sample without the adding of Yb^{3+}. The dependence of the UC emission intensities on the pump power is presented in Figure 4a-4d by the log-log plots. The slopes of the linear fitting are close to 2 for both the Er^{3+}: $^2H_{11/2}$, $^4S_{3/2}\rightarrow{}^4I_{15/2}$ and $^4F_{9/2}\rightarrow{}^4I_{15/2}$ transitions in all the four samples, indicating that two pumping photons are required to populate the $^2H_{11/2}$, $^4S_{3/2}$ and $^4F_{9/2}$ emitting states, respectively.

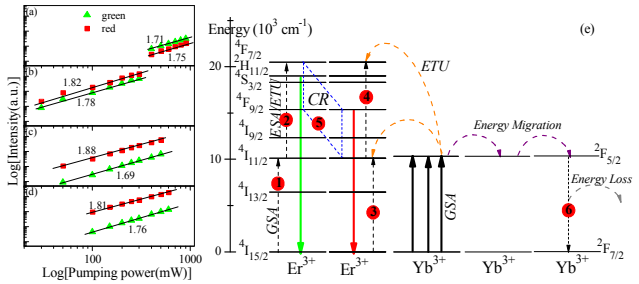

Figure 4 Log-log plots UC intensity versus NIR excitation power for $^2H_{11/2}$, $^4S_{3/2}\rightarrow{}^4I_{15/2}$ and $^4F_{9/2}\rightarrow{}^4I_{15/2}$ transitions of Er^{3+} in GCs: (a) GC0, (b) GC1, (c) GC3 and (d) GC6; (e) energy level diagrams of Er^{3+} and Yb^{3+}, showing possible UC mechanisms in the present samples.

Based on the energy-level diagrams of Er^{3+} and Yb^{3+}, the color-tunable UC mechanisms in the present glass ceramics are proposed, as illustrated in Figure 4e. For GC0 sample without the addition of Yb^{3+}, the electrons in the Er^{3+}: $^4I_{15/2}$ state are promoted to $^4I_{11/2}$ one through ground state absorption (GSA, process 1) under 980 nm laser excitation, then further to $^4F_{7/2}$ via excited state absorption or energy transfer UC (ESA/ETU, process 2) [25]. Afterwards, the $^4S_{3/2}/^4H_{11/2}$ and $^4F_{9/2}$ states are populated by multi-phonon relaxation from $^4F_{7/2}$ one, from which green and red photons yield respectively. Since the energy gap between $^4S_{3/2}/^4H_{11/2}$ and $^4F_{9/2}$ is larger than that between $^4F_{7/2}$ and $^4S_{3/2}/^4H_{11/2}$, non-radiative relaxation probability from $^4S_{3/2}/^4H_{11/2}$ to $^4F_{9/2}$ is lower than that from $^4F_{7/2}$ to $^4S_{3/2}/^4H_{11/2}$, resulting in the dominant green luminescence in GC0 sample. For samples with the introduction of Yb^{3+}, once the sensitizers (Yb^{3+} ions) are populated through ground state absorption (GSA) under NIR excitation, the successive two-step energy transfers (ETs) from Yb^{3+} to Er^{3+} will populate $^4I_{11/2}$ and $^4F_{7/2}$ intermediate states of Er^{3+} (process 3 and process 4). Since the segregation of Ln^{3+} ions in the NCs remarkably decreases the Yb^{3+}-Er^{3+} and Er^{3+}-Er^{3+} distances, energy transfers from Yb^{3+} to Er^{3+} is highly efficient, which results in great population of Er^{3+} $^4I_{11/2}$ and $^4F_{7/2}$ states. Subsequently, cross-relaxation (CR) of $^4F_{7/2}$ + $^4I_{11/2}$ → $^4F_{9/2}$ + $^4F_{9/2}$ between Er^{3+} ions (process 5) [26-28], as depicted in Figure 4e, becomes significant and dominant for realizing the population of Er^{3+}: $^4F_{9/2}$ excited state from which red emission yields. In this case, the more addition of Yb^{3+} ions in the host, the more efficiency of CR process, which will help to concentrate more and more NIR excitation photons in the Er^{3+}: $^4F_{9/2}$ state and result in gradual increase of red/green UC emission ratio. Notably, the gradual decrease of UC emission intensity with high Yb^{3+} content in the samples should be due to the depletion of excitation energy in UC NCs via long-distance energy migration that takes excitation energy to lattice or surface defects by non-radiative relaxation (process 6).

Conclusions

In summary, the Eu^{3+} and Er^{3+} doped transparent GCs containing cubic $K(Y_{1-x}Yb_x)_3F_{10}$ solid-solution NCs were successfully prepared. Different to the cases previously reported, GCs were already formed via self-crystallization during melt-quenching. The obviously Stark splitting emission, the low forced electric dipole $^5D_0\rightarrow{}^7F_2$ transition, and the long decay lifetime of Eu^{3+} evidenced the segregation of lanthanide activators into $K(Y_{1-x}Yb_x)_3F_{10}$. For the Er^{3+} doped GCs, multi-colors such as green, yellow and red UC emissions were achieved by modifying Yb^{3+} content in the Er^{3+}-doped $K(Y_{1-x}Yb_x)_3F_{10}$ NCs embedded GCs under 980 nm laser excitation, ascribing to the low phonon energy environment of lanthanide activators enriched in NCs and the efficient Yb^{3+}-Er^{3+} and Er^{3+}-Er^{3+} inter-ionic interactions.

This work was supported by the National Natural Science Foundation of China (21104068, 21271170, 61372025 and 51402077).

Notes and references

[a] *College of Materials & Environmental Engineering, Hangzhou Dianzi University, Hangzhou, 310018, P. R. China. Fax/Tel: 86-571-87713542; E-mail: dqchen@hdu.edu.cn; jizg@hdu.edu.cn*
[b] *State Key Laboratory of Structural Chemistry, Fujian Institute of Research on the Structure of Matter, CAS, Fuzhou, Fujian 350002, PR China. Fax/Tel: 86-571-87713535; E-mail: phuang@fjirsm.ac.cn*

1 H. A. Höpper, *Angew. Chem. Int. Ed.*, 2009, **48**, 3572.
2 F. Wang, Y. Han, C. Lim, Y. Lu, J. Wang, J. Xu, H. Chen, C. Zhang, M. Hong and X.G. Liu, *Nature*, 2010, **463**, 1061.
3 D. Chen, Y. Wang and M. Hong, *Nano Energy*, 2012, **1**, 73.
4 S. Gai, C. Li, P. Yang and J. Lin, *Chem. Rev.*, 2014, **114**, 2343.
5 J. Wang, R. Deng, M. A. MacDonald, B. Chen, J. Yuan, F. Wang, D. Chi, T. S. Andy Hor, P. Zhang, G. Liu, Y. Han and X. Liu, *Nat. Mater.*, 2014, **13**, 157.
6 D. Q. Chen, W. D. Xiang, X. J. Liang, J. S. Zhong, H. Yu, M. Y. Ding, H. W. Lu and Z. G. Ji. *J. Euro. Ceram. Soc.*, 2015, **35**, 859.
7 Y.H. Wang and J. Ohwaki, *Appl. Phys. Lett.*, 1993, **63**, 3268.
8 F. Liu, E. Ma, D. Q. Chen, Y.L. Yu and Y.S. Wang, *J. Phys. Chem. B*, 2006, **110**, 20843.
9 F. Liu, Y. S. Wang, D. Q. Chen, Y.L. Yu, E. Ma and P. Huang, *Mater. Lett.*, 2007, **61**, 5022.
10 D. Q. Chen, Y. S. Wang, Y. Yu, F. Liu and P. Huang, *App. Phys. Lett.*, 2007, **91**, 051920.
11 D. Q. Chen, Y. S. Wang, K. L. Zheng, T. L. Guo, Y. L. Yu and P. Huang, *App. Phys. Lett.*, 2007, **91**, 251903.
12 S. Ye, B. Zhu, J. Chen, J. Luo and J. R. Qiu, *Appl. Phys. Lett.*, 2008, **92**, 141112.
13 D. Q. Chen, Y.L. Yu, P. Huang, F. Y. Weng, H. Lin and Y. S. Wang, *Appl. Phys. Lett.*, 2009, **94**, 041909.
14 S. Bhattacharyya, C. Bocker, T. Heil, J. R. Jinschek, T. Höche, C. Rüssel and H. Kohl, *Nano. Lett.*, 2009, **9**, 2493.
15 A.C. Yanes, A. Santana-Alonso, J. Méndez-Ramons, J. del-Castillo and V.D. Rodríguez, *Adv. Funct. Mater.*, 2011, **21**, 3136.
16 A. Herrmann, M. Tylkowski, C. Bocker and C. Rüssel, *Chem. Mater.*, 2013, **25**, 2878.
17 S. L. Zhao, X. L. Wang, X. Sun, G. H. Jia, L. H. Huang, D. G. Deng, F. X. Xin and S. Q. Xu, CrystEngComm, 2013, 15, 7346.
18 A. Herrmann, M. Tylkowski, C. Bocker and C. Rüssel, *J. Mater. Sci.*, 2013, **48**, 6262.
19 Y. L. Wei, H. M. Yang, X. M. Li, L. J. Wang and H. Guo, *J. Am. Ceram. Soc.*, 2014, **97**, 2012.
20 V. Mahalingam, F. Vetrone, R. Naccache, A. Speghini, J. A. Capobianco, *J. Mater. Chem.*, 2009, **19**, 3149.
21 X. Xue, M. Liao, R. N. Tiwari, M. Yoshimura, T. Suzuki, Y. Ohishi, *Appl. Phys. Express*, 2012, **5**, 092601.
22 N. Kodama and Y. Watanabe, *Appl. Phys. Lett.*, 2004, **84**, 4141.
23 L. Zhu, J. Meng and X. Cao, *Mater. Lett.*, 2008, **62**, 3007.
24 D.Q. Chen, Y.L. Yu, P. Huang, H. Lin, Z. Shan and Y.S. Wang, *Acta Mater.*, 2010, **58**, 3035-41.
25 J.P. Vander Ziel, L. G. Van Uitert, W. H. Grodkiewicz and R. M. Mikulgak, *J. Appl. Phys.*, 1986, **60**, 4262.
26 F. Vetrone, J. C. Boyer, J. A. Capobianco, A. Speghini and M. Bettinelli, *J. Appl. Phys.*, 2004, **96**, 661.
27 G. Dantelle, M. Mortier, G. Patriarche and D. Vivien, *J. Solid State Chem.*, 2006, **179**, 1995.
28 S. Zeng, G. Ren and Q. Yang, *J. Mater. Chem.*, 2010, **20**, 2152.